Aerospace Science and Technology 93 (2019) 105181

Contents lists available at ScienceDirect

Aerospace Science and Technology

www.elsevier.com/locate/aescte

Civil turbofan engine exhaust aerodynamics: Impact of fan exit flow characteristics

Ioannis Goulos [a,*], David MacManus [a], Christopher Sheaf [b]

[a] Propulsion Engineering Centre, School of Aerospace Transport and Manufacturing, Cranfield University, Bedfordshire, MK43 0AL, UK
[b] Installation Aerodynamics, Rolls-Royce plc, Trent Hall 2.2, Derby, DE24 8BJ UK

ARTICLE INFO

Article history:
Received 30 August 2018
Received in revised form 25 February 2019
Accepted 12 May 2019
Available online 17 May 2019

ABSTRACT

It is envisaged that future civil aero-engines will operate with greater bypass ratios compared to contemporary configurations to lower specific thrust and improve propulsive efficiency. This trend is likely to be accompanied with the implementation of a shorter nacelle and bypass duct for larger engines. However, a short bypass duct may result in an aerodynamic coupling between the exit flow conditions of the fan Outlet Guide Vanes (OGVs) and the exhaust system. Thus, it is imperative that the design of the exhaust is carried out in combination with the fan exit profile. A parabolic definition is used to parameterise and control the circumferentially-averaged radial profiles of stagnation pressure and temperature at the fan OGV exit. The developed formulation is coupled with a parametric exhaust design approach, an automatic computational mesh generator, and a compressible flow solution method. A global optimisation strategy is devised comprising methods for Design of Experiment (DOE), Response Surface Modelling (RSM), and genetic optimisation.

A combined Design Space Exploration (DSE) comprising both geometric, as well as fan exit profile variables, is performed to optimise the exhaust geometry in conjunction with the fan exit profile. The developed approach is used to derive optimum exhaust geometries for a tip, mid, and hub-biased fan blade loading distribution. It is shown that the proposed formulation can ameliorate adverse transonic flow characteristics on the core after-body due to a non-uniform bypass inflow. The hub-loaded profile was found to be most penalising in terms of exhaust performance compared to the mid and tip-loaded variants. It is demonstrated that the combined fan exit profile and exhaust geometry optimisation offers significant performance improvement compared to the fixed inflow cases. The predicted performance benefits can reach up to 0.19% in terms of exhaust velocity coefficient, depending on fan loading characteristics. A notable improvement is also noted in terms of bypass nozzle discharge coefficient. This suggests that the combined optimisation can lead to an exhaust design that can satisfy the engine mass-flow rate demand with a reduced geometric throat area, thus potentially offering further exhaust size and weight benefits.

1. Introduction

1.1. Background

It is envisaged that the next generation of large civil aero-engines will operate with substantially greater values of By-Pass Ratio (BPR) compared to contemporary architectures in order to lower specific thrust and improve propulsive efficiency [1,2]. This trend results in a higher gross to net propulsive force ratio, $\frac{F_G}{F_N}$, which changes from approximately 3 to 4 for increasing the value of *BPR* from 11 to 15+ at a fixed cycle technology level and F_N [3]. However, the aerodynamic behaviour of the exhaust system has a first-order effect on gross propulsive force F_G [4]. Hence, it is anticipated that the performance of the exhaust system will play an increasingly important role to the success of future Very-High-Bypass-Ratio (VHBR) civil aero-engines.

An increase in BPR is likely to be accompanied with the implementation of a shorter nacelle and bypass duct to ameliorate the adverse impact of large engine installation effects [5–7]. However, a short bypass duct may result in a comparatively stronger aerodynamic coupling between the flow conditions at the fan exit and the aerodynamic behaviour of the exhaust system [8]. Thus, it is imperative that the exhaust design space is explored in an inte-

* Corresponding author.
E-mail address: i.goulos@cranfield.ac.uk (I. Goulos).

https://doi.org/10.1016/j.ast.2019.05.033

Nomenclature

Roman Symbols

a, b, c	Parabolic equations coefficients
C_D^{Bypass}	Bypass exhaust nozzle discharge coefficient
C_D^{Core}	Core exhaust nozzle discharge coefficient
$C_V^{Overall}$	Exhaust system overall velocity coefficient
F_G, F_N	Gross and net propulsive force, ... N
k	Turbulent kinetic energy, ... m^2/sec^2
L, R	Length and Radius, ... m
M_∞	Free-stream Mach number
$N_{Pearson}$	Pearson's product-moment of correlation
P, T	Pressure and Temperature, ... Pa and K
r	Normalised radial coordinate, $= \frac{R - R_{OGV}^{min}}{R_{OGV}^{max} - R_{OGV}^{min}}$
r_{P_0/T_0}^{max}	Normalised radial coordinate of maximum P_0, T_0
SF	Parabolic equation amplitude scaling factor
x, y	Parabolic equation variables

Greek Symbols

κ, h	Parabolic shape control vertex coordinates
ω	Specific dissipation rate, ... 1/sec
θ_{sw}^{avg}	Area-averaged fan OGV exit swirl angle, ... deg

Superscripts

avg	Referring averaged flow conditions
$Bypass$	Referring to the bypass exhaust system
$Core$	Referring to the core exhaust system
min/max	Referring the minimum or maximum position
$Overall$	Referring to the overall exhaust system

Subscripts

0	Referring to stagnation flow conditions
CP	Referring to the nozzle charging plane
$Exit$	Referring to the nozzle exit plane
OGV	Referring to the fan OGV exit plane
st	Referring to static flow conditions

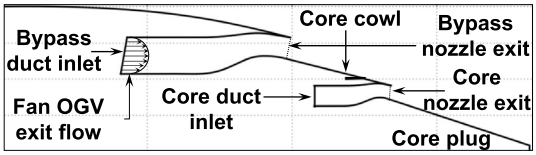

Fig. 1. Notional housing geometry for a turbofan engine equipped with separate-jet exhausts.

grated manner and that the combined Low-Pressure (LP) system is optimised at engine level during preliminary design. This practice entails the design of the exhaust to be carried out in conjunction with the aerodynamic characteristics at the fan exit to maximise the LP exhaust flow-path efficiency.

Within this work, the term "exhaust system" is used to denote the bypass and core ducts and nozzles including their respective after-bodies. An air-flow vent is usually located on the core after-body, also referred to as the "core cowl", and is used to exhaust secondary air-flows. The geometry of a notional separate-jet exhaust for a civil turbofan engine is shown in Fig. 1.

The design optimisation of separate-jet exhausts for civil aero-engines has been reported by Goulos et al. [3,9–11]. However, previous analyses [3,9–13] have neglected the aerodynamic coupling between the fan exit flow distribution and the bypass exhaust system. As a result, the impact of inflow non-uniformity at the bypass duct inlet (Fig. 1) has been traditionally omitted during the preliminary design of aero-engine exhaust systems. However, previous investigations have shown that the radial variations of total pressure P_0 and temperature T_0 at the bypass inlet can influence the aerodynamic behaviour of the exhaust system [14]. As a result, the assumption of uniform inlet conditions could potentially lead to the design of exhaust geometries that are sub-optimum when operated using a realistic inlet flow-field.

1.2. Exhaust performance prediction and accounting

The aerodynamic forces exerted on the walls of an aero-engine exhaust system affect the produced gross propulsive force F_G. Dusa et al. [15] noted that the reduction in F_G due to non-isentropic flow phenomena can be of the order of 1.5–2.0% relative to the case of isentropic flow. The aerodynamic performance of an exhaust system is usually referred to that of an ideal nozzle using the non-dimensional discharge and velocity coefficients, C_D and C_V, respectively [16,17].

1.3. LP exhaust flow-path optimisation for civil aero-engines

There is a dearth of literature that deals with the optimisation of the bypass exhaust system in conjunction with the aerodynamic characteristics of the fan design. It is noted that substantial research has been reported to date on the aerodynamic design and optimisation of low-speed [18] and transonic fan configurations [19,20] for aero-engines. However, the impact of fan blade span-wise loading on the aerodynamic behaviour of the bypass duct and nozzle has not been investigated to date. This aspect is of increasing interest due to the importance of the exhaust system in ensuring the success of future VHBR aero-engines [10,11]

Clement et al. [21] reported on the optimisation of the LP exhaust system for a high BPR civil turbofan engine. The employed topology included the fan OGVs, the bypass duct, as well as structural components such as struts, fairing, and bifurcations. The bypass duct geometry was parameterised using second-order splines, whilst the 3D Reynolds-Averaged Navier-Stokes (RANS) flow-solver HYDRA[22] was used to carry out the aerodynamic analyses. A holistic optimisation strategy was devised including methods for DOE, surrogate modelling, and global optimisation. A random sequence generator[23] was incorporated to sample the prescribed design space, whilst interpolation using Radial Basis Functions (RBF)[24] was deployed to structure the required surrogate models. A Genetic Algorithm (GA) [25] was applied to optimise the exhaust geometry by minimising the total pressure loss in the bypass duct. The combined process was able to reduce the predicted total pressure loss within the duct by 0.1% relative to a baseline design.

Tschirner et al. [26] developed an automated aerodynamic analysis process, based on Computational Fluid Dynamics (CFD), for the minimisation of aerodynamic losses generated in the fan OGVs and downstream struts by the introduction of a core mount arm. A RANS method was applied on a hybrid structured–unstructured grid using the Spalart–Allmaras turbulence model [27]. An extensive optimisation campaign was carried out to identify an optimum combination of pylon, strut fairing, and OGV stagger angle that minimised total pressure loss in the bypass exhaust whilst keeping the circumferential pressure distortion to an acceptable value.

Keith et al. [12] described an integrated framework targeting the aerodynamic analysis of three-dimensional (3D) separate-

jet exhaust systems for turbofan engines. Their numerical approach was based on CFD through the deployment of a RANS scheme [28]. Flow-field analyses were carried out and reported for two-dimensional (2D) axi-symmetric exhaust geometries as well as for 3D designs including the bifurcations and pylon. Keith et al. concluded that the exhaust flow properties for the axi-symmetric cases are representative of those corresponding to the full 3D designs with respect to regions away from the influence of the bifurcations and pylon. However, the impact of P_0 and T_0 radial profiles downstream of the fan OGV exit was not accounted for in the reported analyses.

1.4. Scope of present work

This paper reports the development of an integrated approach for the LP exhaust flow-path optimisation of civil aero-engines during preliminary design. The method is able to evaluate the impact of fan exit flow characteristics on the aerodynamically optimum exhaust shape, as well as to optimise the exhaust geometry and fan exit profile simultaneously. The developed approach extends previous work [3,9] through the parametric representation of non-uniform flow conditions at the fan OGV exit. A parabolic mathematical definition is employed to parameterise and control the radial distributions of P_0 and T_0 for fixed averaged flow properties. The developed formulation is coupled with a parametric exhaust design method [3], an automatic mesh generator [29], and a Favre-averaged flow solution method [30]. A computationally efficient optimisation strategy is adapted comprising numerical methods for Design Space Exploration (DSE) [31], Response Surface Modelling (RSM) [32], and genetic optimisation [33]. The DSE approach is extended to include the fan OGV exit flow control variables in combination with the previously employed geometric control variables [11]. This enables the identification of optimised radial flow profiles for any exhaust geometry, or the derivation of exhaust designs optimised for specific inlet conditions, as well as any combination of the above.

The developed method is employed to investigate the impact of three fan OGV exit profiles on the performance of a VHBR engine exhaust system, reflecting different types of fan blade span-wise loading. These correspond to tip, mid, and hub-loaded fan blade designs. A comparative evaluation is initially performed to identify the underlying flow mechanisms that govern the impact of fan OGV exit profile on the aerodynamic behaviour of the exhaust system. An aerodynamic DSE is carried out to quantify the influence of inlet non-uniformity magnitude and radial flow biasing on the exhaust performance metrics of interest. Subsequently, a DOE comprising both exhaust geometry and fan exit profile variables, is deployed to populate a combined design database used for surrogate modelling purposes. The structured RSMs are incorporated to carry out a combined inflow and geometry optimisation in order to obtain a globally optimum combination of fan exit profile and exhaust design. A set of optimised exhaust geometries are also derived for fixed fan OGV exit flow conditions corresponding to each fan blade loading type. The obtained results are used to derive performance change estimates due to the inflow constraints associated with the investigated types of fan blade loading.

2. Numerical approach

This work is based on the mathematical method originally developed by Goulos et al. [3,9–11] for the aerodynamic analysis of civil turbofan engines with separate-jet exhausts. The developed approach has been named GEMINI (**G**eometric **E**ngine **M**odeller **I**ncluding **N**ozzle **I**nstallation). GEMINI can automatically design, mesh, simulate, and optimise the geometry of an exhaust system based on a designated engine cycle and a limited set of key hard points prescribed by the user. GEMINI encompasses a series of fundamental modelling methods originally developed for; engine performance analysis [34], exhaust duct and nozzle aeroline parameterisation [3,35,36], RANS flow solution [29,30], as well as DSE [31,32] and Multi-Objective Optimisation (MOO) [33]. An analytical description of the individual modules has been provided by Goulos et al.[3,9–11]. Therefore, only a brief synopsis of the system is provided.

2.1. GEMINI: Aerodynamic design and analysis of civil aero-engine exhaust systems

The exhaust design method in GEMINI commences by evaluating the aero-thermal behaviour of the engine. This includes both Design Point (DP) as well as Off-Design (OD) conditions. Aero-thermal analysis is carried out using the 0D method TURBOMATCH, originally described by Macmillan [34]. The purpose of this process is two-fold: (a) it estimates the throat-area demand for the bypass and core nozzles, and (b) it determines the averaged flow properties at the inlet of each nozzle to be used as Boundary Conditions (BCs) in the CFD analysis. TURBOMATCH has been used in several studies in the literature for the prediction of DP, OD, and transient performance of gas turbine engines [37].

Having established the key engine area requirements from the 0D aero-thermal analysis, GEMINI produces the aerodynamic lines for the engine components such as the nacelle and the exhaust system (Fig. 1). An automated mesh generation method is subsequently deployed to establish a multi-block structured mesh [29]. This defines the computational domain upon which the viscous and compressible flow-field are resolved [30]. The obtained CFD solutions are subsequently post-processed to derive the exhaust performance metrics [3]. These include the bypass and core nozzle discharge coefficients, C_D^{Bypass} and C_D^{Core}, respectively, and the overall exhaust velocity coefficient $C_V^{Overall}$.

All boundary-layer blocks within the computational domain are discretised to employ a total of 50 nodes normal to the wall surface, as well as to satisfy a y^+ value below unity for all wall-adjacent cells. A growth ratio of 1.2 is applied for the inflation of the boundary-layer nodes normal to each viscous wall surface. A grid independence analysis was carried out and reported by Goulos et al. [3] where the associated Grid Convergence Indices (GCI) for C_D^{Bypass}, C_D^{Core}, and $C_V^{Overall}$ were shown to be approximately 0.017%, 0.83%, and 0.058%, respectively, for a mesh with a total of 4.75×10^5 elements. However, it is noted that the meshes used within this work featured approximately 8×10^5 elements.

A Favre-Averaged CFD approach [30] coupled with the $k-\omega$ Shear-Stress Transport (SST) turbulence model [38] is employed for all computations reported in this article. The Green-Gauss node-based method is utilised for calculation of the flow-field gradients. A second-order accurate upwind scheme is used for the spatial discretisation of primitive variables as well as turbulent kinetic energy k and specific dissipation rate ω. Kinetic theory [39] is applied for the computation of thermal conductivity. Variable gas properties are employed based on an $8th$ order piece-wise polynomial expression for the estimation of specific heat capacity as a function of T_{st}. Sutherland's law [40] is applied for the computation of dynamic viscosity. All viscous walls are treated as adiabatic whilst non-reacting flow conditions are assumed. The employed CFD approach was verified and validated by Goulos et al. [3] and Otter et al. [41].

With this numerical approach, the relative percentage difference in mass-flow between the bypass duct inlet and the bypass nozzle outlet was of the order of 0.01%, with similar values estimated for the core nozzle. However, this relative error is more than an order of magnitude below the percentage differences noted in

$C_V^{Overall}$ and C_D^{Bypass} due to the impact of fan loading characteristics, as shown in Figs. 4 and 9, within section 3 of this article.

2.2. Exhaust system parametric design

GEMINI incorporates a parametric geometry definition based on the Class-Shape function Transformation (CST) method originally proposed by Kulfan [35] and further developed by Qin [36]. The employed approach developed by Goulos et al. [3] inherits the intuitiveness and flexibility of Qin's CST variation [36] and extends its applicability to the parametric representation of exhaust ducts, nozzles, and after-bodies [10]. The adapted formulation allows to express the bypass/core duct, nacelle exhaust, and after-body aerolines as functions of intuitive parameters. The employed parametric geometry definition has been extensively described by Goulos et al. [3,10,11].

2.3. Parametric fan OGV exit flow representation

To mitigate the excessive computational overhead associated with modelling the complex three-dimensional flow-field within the fan stage, a reduced-order model is developed for the parametric representation of the radial flow properties at the fan OGV exit. This is accomplished through the use of a parabolic definition for the parameterisation and control of the circumferentially averaged radial distributions of P_0 and T_0 immediately downstream of the fan OGV exit.

The fundamental mathematical definition of a generic parabolic equation can be expressed as follows [42]:

$$y(x) = a(x-h)^2 + \kappa \tag{1}$$

where the coefficient a represents the amplitude of the parabola, whilst the parameters κ and h denote the coordinates of the shape control vertex in the Cartesian plane. Since the parabolic definition is used to control radial flow variations, the independent coordinate x in Eq. (1) is reassigned to the normalised radial coordinate at the fan OGV exit; $r = \dfrac{R - R_{OGV}^{min}}{R_{OGV}^{max} - R_{OGV}^{min}}$ where $r \in [0,1]$. It is noted that R_{OGV}^{max} and R_{OGV}^{min} signify the minimum and maximum radii at the fan OGV exit, respectively, whilst R corresponds to the local radial coordinate with $R \in [R_{OGV}^{min}, R_{OGV}^{max}]$. The vertex control coefficients κ and h are uniquely related to the maximum distribution value $(y(r)^{max})$ and its corresponding independent radial coordinate $r(y(r)^{max}) = r_y^{max}$, respectively. Thus, for the case of P_0 it follows that $P_0(r) = y(r)$, $P_0^{max} = \kappa$, and $r_{P_0}^{max} = h$, with similar expressions used for T_0. With these provisions, Eq. (1) can be expanded and re-written in a non-dimensional manner as described below:

$$\frac{P_0(r)}{P_0^{avg}} = ar^2 - 2ar_{P_0}^{max} r + \left(a \times (r_{P_0}^{max})^2 + \frac{P_0^{max}}{P_0^{avg}} \right) \tag{2}$$

where normalisation is carried out with respect to the axi-symmetrically area-weighted average total pressure P_0^{avg}. Equation (2) follows the standard parabolic equation form of $y(x) = ax^2 + bx + c$, whereby the polynomial coefficients are given by:

$$b = -2ar_{P_0}^{max} \tag{3a}$$

$$c = a \times (r_{P_0}^{max})^2 + \frac{P_0^{max}}{P_0^{avg}} \tag{3b}$$

For $r_{P_0}^{max} \in [0,1]$, the expression used for the determination of coefficient a in the RHS of Eq. (2), which represent the amplitude of the parabolic definition, is dependent on $r_{P_0}^{max}$ as shown below:

$$a = SF \times \frac{-\dfrac{P_0^{max}}{P_0^{avg}}}{(r_{P_0}^{max})^2 - 2r_{P_0}^{max} + 1}, \quad for \quad r_{P_0}^{max} < 0.5 \tag{4a}$$

$$a = SF \times \frac{-\dfrac{P_0^{max}}{P_0^{avg}}}{(r_{P_0}^{max})^2}, \quad for \quad r_{P_0}^{max} \geq 0.5 \tag{4b}$$

where SF is a numerically derived factor required to ensure scalability. Equation (2) describes the radial distribution of normalised total pressure $\left(\dfrac{P_0(r)}{P_0^{avg}}\right)$ at the fan OGV exit as a function of solely two parameters: (a) the maximum value of normalised total pressure $\left(\dfrac{P_0^{max}}{P_0^{avg}}\right)$, and (b) the corresponding radial location $r_{P_0}^{max}$ where the peak value of P_0 manifests.

It is noted that direct application of Eq. (2) yields non-negligible variations in the area-weighted average value of $P_0(r)$, noted above as P_0^{avg}. As a result, Eq. (2) is essentially non-scalable as it does not automatically conserve P_0^{avg} when P_0^{max} and $r_{P_0}^{max}$ are explicitly varied. Thus, a further provision is required to ensure scalability so that the employed parameterisation satisfies the conservation of area-averaged flow properties. This is established through the application of an iterative scheme used to adjust the amplitude of the parabola through the scaling factor SF in Eqs. (4a) and (4b). The condition used to determine SF dictates that the area-averaged normalised total pressure distribution over the axi-symmetric annulus must be equal to unity. This can be expressed through the following equation:

$$\int_0^1 \left(\frac{P_0(r)}{P_0^{avg}}\right) r dr + \frac{R_{OGV}^{min}}{R_{OGV}^{max} - R_{OGV}^{min}} \times \int_0^1 \left(\frac{P_0(r)}{P_0^{avg}}\right) dr - \frac{R_{OGV}^{max} + R_{OGV}^{min}}{2(R_{OGV}^{max} - R_{OGV}^{min})} = 0 \tag{5}$$

Equation (5) is a scalar non-linear equation that can be solved numerically for the unknown value of SF using an appropriate solution scheme such as the bisection or Newton's method. The numerical solution of Eq. (5) and subsequent use of Eqs. (4a, 4b), (3a, 3b) and Eq. (2) automatically result in the area-averaged radial distribution of normalised total pressure $\left(\dfrac{P_0(r)}{P_0^{avg}}\right)$ for prescribed values of $\left(\dfrac{P_0^{max}}{P_0^{avg}}\right)$ and $r_{P_0}^{max}$. The derived distribution can be subsequently scaled to reflect the dimensional variation of $P_0(r)$ using a specific value of area-averaged total pressure P_0^{avg}. The developed approach was also used throughout this paper to prescribe boundary conditions at the bypass inlet in terms of $T_0(r)$. A least-squares-based interpolation scheme was employed to apply discrete P_0 and T_0 values at the bypass inlet grid points (Fig. 1) based on the derived analytical variations of $P_0(r)$ and $T_0(r)$.

An example of this process is illustrated in Fig. 2. Fig. 2(a) demonstrates that the parameterisation can be employed to control the magnitude of non-uniformity of a radial profile through specification of the maximum to area-averaged value of a designated flow property. The method can approximate the radial distributions of P_0 at the fan OGV exit using representative numerical values for $\left(\dfrac{P_0^{max}}{P_0^{avg}}\right)$ and $r_{P_0}^{max}$ extracted from computationally or

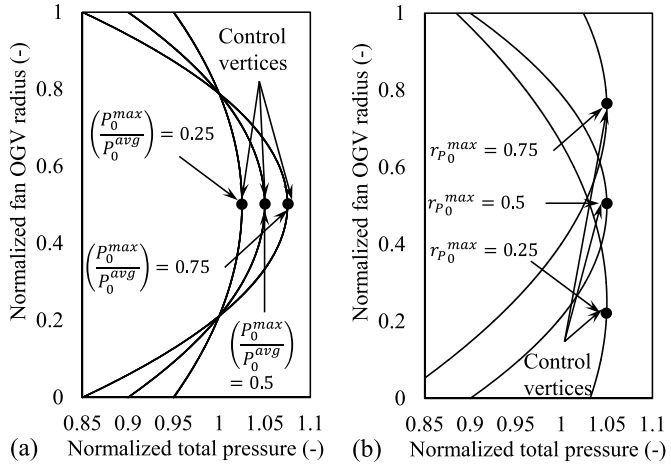

Fig. 2. Normalised radial profiles of $P_0(r)/P_0^{avg}$: (a) impact of $\left(\frac{P_0^{max}}{P_0^{avg}}\right)$ for $r_{P_0}^{max} = 0.5$, (b) impact of $r_{P_0}^{max}$ for $\left(\frac{P_0^{max}}{P_0^{avg}}\right) = 1.05$.

experimentally derived radial traverses of P_0 found in the literature [43]. Fig. 2(b) shows that the developed parametric inflow definition can be used to model the radial flow distributions of P_0 for representative hub-loaded ($r_{P_0}^{max} = 0.25$), mid-loaded ($r_{P_0}^{max} = 0.5$), and tip-loaded ($r_{P_0}^{max} = 0.75$) fan designs.

The selection of area-weighted averaging in the derivation of Eq. (5) as opposed to the commonly employed momentum-weighted and mass-weighted averaging [44] techniques, is due to the unknown radial variations of mass, momentum, and enthalpy fluxes at the fan OGV exit prior to a CFD analysis. This is due to the impact of the exhaust geometry and nozzle base-pressure on the radial static pressure distribution at the bypass inlet [14]. The proposed approach employs area-weighted averaging to ensure consistent application of P_0 and T_0 BCs at the fan OGV exit in a manner that is independent of exhaust design and does not entail an a-priori CFD analysis. However, to maintain consistency with standard practice in terms of exhaust analysis [3,17,44], the mass-averaged values of P_0 and T_0 and the bypass inlet are calculated a-posteriori of the aerodynamic evaluation and subsequently used for the evaluation of the exhaust metrics; $C_V^{Overall}$, C_D^{Bypass}, and C_D^{Core}. However, Bucci [14] showed that for inflow definition parameters in terms of $\left(\frac{P_0^{max}}{P_0^{avg}}\right)$ and $\left(\frac{T_0^{max}}{T_0^{avg}}\right)$ reflecting realistic mid-loaded profiles, the associated percentage differences for P_0 and T_0 between mass and area averaging are below 0.5% and 0.15%, respectively.

The employed parametric inflow definition was developed to approximate the bulk-flow parameters in terms of P_0 and T_0 radial profiles at the fan exit. These were based on representative experimental or numerical flow distributions found in the literature [43,45]. It is emphasised that the ultimate goal of this work is the development of a rapid methodology that allows for the design of the exhaust to be carried out in combination with the design of the fan. From this perspective, the fan blade span-wise loading directly affects the fan exit flow profile, which has an impact on the performance of the exhaust. Concurrently, the employed inflow definition was selected for its capacity to represent primarily the impact of any designated fan blade span-wise loading on the radial profiles of P_0 and T_0 at the bypass duct inlet, as shown in Fig. 1.

Furthermore, this method was selected for its ability to parametrically reproduce fan exit flow profiles using a reduced number of variables, thus maintaining low-dimensionality and ensuring applicability in a DSE environment. It was shown in Fig. 2 that this inflow definition can be used to control the span-wise variation of $P_0(r)/P_0^{avg}$ using only two parameters: $\left(\frac{P_0^{max}}{P_0^{avg}}\right)$ for $r_{P_0}^{max}$. Identical expressions are used for the parametric definition of $T_0(r)/T_0^{avg}$. As such, it is a flexible and efficient approach that can be used to model the impact of fan blade span-wise loading on the P_0 and T_0 profiles at the bypass inlet. Hence, the combined approach can be used to directly relate the impact of changes in fan blade span-wise loading on the aerodynamic performance of the exhaust.

However, it recognised that this approach does not account for certain non-uniformities in the circumferentially-averaged flow-field at the fan exit due to the presence of flow-features such as near-wall boundary-layer momentum deficit, hub and tip secondary flows, and tip-leakage flows. As such, the impact of these flow-features on the radial variation of P_0 and T_0 is not modelled in this work.

2.4. Design space exploration and optimisation

GEMINI employs a computationally efficient optimisation strategy based on surrogate-modelling that accounts for the inherent non-linearity of transonic flow aerodynamics and reduces the computational overhead cost with multiple CFD evaluations [9]. The approach has been extensively described by Goulos et al. [9], thus only a brief synopsis will be provided in this paper.

GEMINI comprises modules for DSE, RSM (also referred to as surrogate modelling), parameter identification, and MOO. The DSE method comprises two parts; (a) an initial DOE which strategically populates the design space, and (b) the derivation of RSMs using the DOE sample data. The Latin Hypercube Design (LHD) DOE algorithm [31] has been selected for this work. Having completed the computational process driven by the LHD DOE, RSMs can be structured using the sample data as model inputs. Interpolation using Gaussian Processes Regression [32] (Kriging Interpolation) is used in this work.

The derived RSMs can be used to predict the aerodynamic behaviour of new LP systems including the impact of both inflow and exhaust geometry definition parameters. GEMINI incorporates RSMs as drivers during the optimisation process instead of relying directly on CFD analysis. The underlying purpose is to mitigate the excessive computational overhead associated with numerous CFD evaluations. The Leave-One-Out (LOO) cross-validation method [46] is deployed to evaluate the predictive accuracy of the structured RSMs. The Non-dominated Sorting Genetic Algorithm II (NSGA-II) originally proposed by Deb et al. [33] was the optimiser of choice due to its global convergence characteristics. Due to the deployment of surrogate models in the optimisation, a novel approach is incorporated that is able to track and suppress the uncertainty associated with RSM predictions. The method is able to identify potential RSM deficiencies and mitigate their impact in the pursuit of optimum solutions.

Within this work, the employed DSE and MOO approach of GEMINI has been further extended to include the associated fan OGV exit flow control variables for P_0 and T_0 (Fig. 2) in combination with the previously employed geometric control variables [11]. Thus, contrary to a strictly geometric optimisation, as was reported in earlier references [9–11], the newly-developed method can optimise the exhaust geometry and fan OGV flow profiles simultaneously.

3. Results and discussion

A numerical investigation was carried out to evaluate the impact of fan OGV exit profile on the aerodynamic behaviour of the

Table 1
Investigated fan exit profile parameters.

Profile type/Parameter	$\frac{P_0^{max}}{P_0^{avg}}$	$r_{P_0}^{max}$	$\frac{T_0^{max}}{T_0^{avg}}$	$r_{T_0}^{max}$
Tip-loaded	1.062	0.62	1.01	0.62
Mid-loaded	1.074	0.50	1.01	0.50
Hub-loaded	1.075	0.28	1.01	0.28

exhaust system. Furthermore, a holistic DSE campaign was performed to understand the exhaust geometry changes required to accommodate the bypass inflow aerodynamic characteristics associated with prescribed fan blade loading distributions. The investigated power-plant architecture was defined to be representative of future large turbofans [1]. Aerodynamic analyses were carried out for a VHBR civil aero-engine with $BPR \approx 16$, $FNPR \approx 2.2$, and $CNPR \approx 1.5$ at DP mid-cruise conditions ($M_\infty = 0.85$, $Alt. =$ 10668 m). The engine cycle was compiled based on publicly available information for a "year 2025 to 2030" entry to service technology level [47]. The cycle derivation approach was documented by Goulos et al. [10].

3.1. Aerodynamic impact of fan exit flow profile

A parametric analysis was initially carried out to understand the flow mechanisms associated with the effect on fan OGV exit profile on exhaust aerodynamics. Numerical analyses were performed for three distributions of $P_0(r)$ and $T_0(r)$ reflecting different types of fan blade loading. These correspond to tip, mid, and hub-loaded designs. The associated profile control parameters are documented in Table 1. The baseline profiles were defined to have increased non-uniformity magnitude in terms of $\frac{P_0^{max}}{P_0^{avg}}$ to better show-case the impact of adverse flow features associated with each type of fan-blade loading. Bucci [14] showed that the impact of $T_0(r)$ on the aerodynamic behaviour of the exhaust is an order of magnitude smaller compared to the influence of $P_0(r)$. Hence, the focus of this work is on $P_0(r)$, whilst the associated changes in $T_0(r)$ are tailored accordingly to establish flow compatibility in terms of fan blade loading, as outlined in Table 1.

The baseline exhaust geometry is equipped with convergent bypass and core nozzles and was pre-optimised at DP mid-cruise conditions for $C_V^{Overall}$ as described by Goulos et al. [11] using a notional mid-loaded fan OGV exit flow profile with $\left(\frac{P_0^{max}}{P_0^{avg}}\right) \approx 1.02$ and $r_{P_0}^{max} \approx 0.52$. Fig. 3 presents the impact of the defined parabolic profiles (Table 1) on the aerodynamic behaviour of the baseline exhaust. Numerical results are presented for the tip, mid, and hub-loaded variants in Figs. 3(b), (c), and (d), respectively, whilst Fig. 3(a) illustrates the exhaust flow-field for the case of uniform bypass inflow. The corresponding distributions of $P_0(r)$ at the bypass duct entry are also shown in Figs. 3(a)-(d).

Fig. 3(a) demonstrates that for the case of uniform inflow, the aerodynamic behaviour of the pre-optimised exhaust does not exhibit any notable adverse flow features. The subsonic flow within the bypass duct is fully attached whilst the bypass nozzle operates choked with a clearly defined sonic line. The flow over the core cowl is fully supersonic until the vicinity of the trailing edge. A transonic flow pattern of relatively weak oblique shocks and expansion fans manifests downstream of the core cowl trailing edge which gradually aligns the bypass flow with the axial direction. Furthermore, the occurrence of weak locally supersonic flow domains can be observed on the bypass nozzle inner annulus between the CP and the nozzle exit. This is due to the inner wall curvature distribution that has been pre-optimised for a non-uniform profile with reduced P_0 content near the inner wall [11].

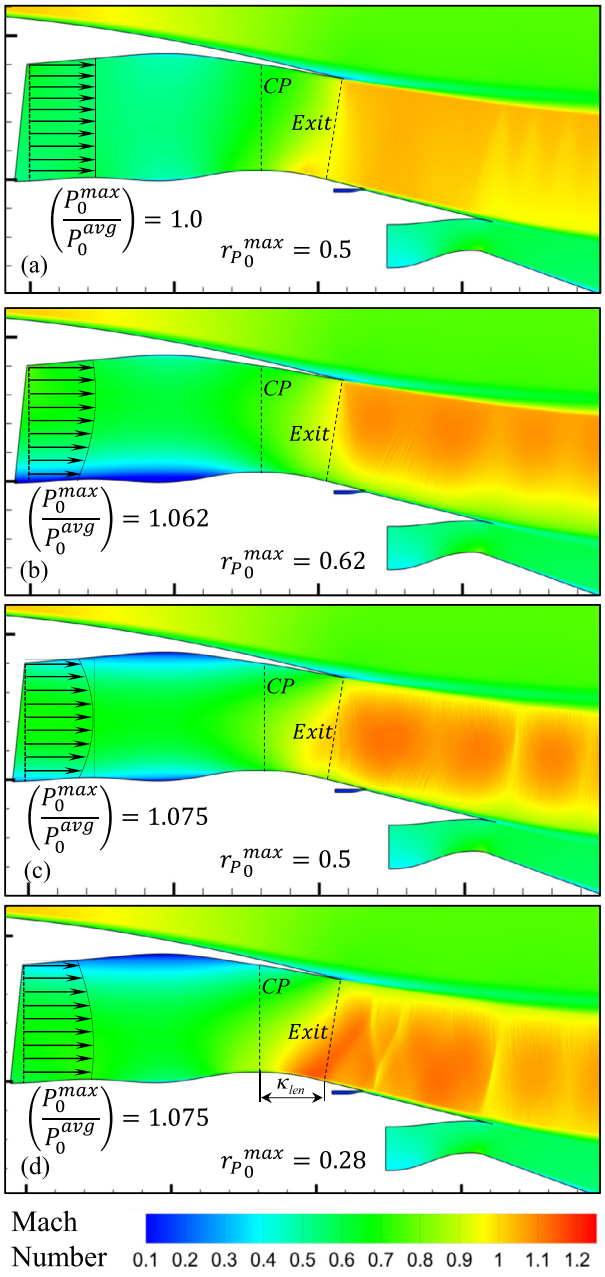

Fig. 3. Impact of fan exit profile on exhaust aerodynamics: (a) uniform inflow, (b) tip-loaded, (c) mid-loaded, and (d) hub-loaded.

Fig. 3(b) demonstrates that a tip-loaded profile has led to a region of low momentum flow near the inner annulus wall which extends from the bypass duct entry to the nozzle charging plane (CP). This is due to the P_0 deficit of the tip-loaded profile near the inner annulus, combined with the adverse pressure gradient that naturally manifests within that region due to a diffusive duct geometry [11]. The combination of these flow-features can result in extended regions of flow separation near the inner duct annulus wall which has an adverse impact on exhaust performance. Furthermore, it can be noted that the bypass flow at the nozzle exit has become locally subsonic at the inner annulus due to the reduced P_0 content. Although the specific flow feature may not directly result in a significant performance penalty, it can affect fan compatibility if present during DP mid-cruise conditions.

The effect of a mid-loaded profile on the exhaust aerodynamics is presented in Fig. 3(c). It can be observed that the specific profile has resulted in a reduction of near-wall velocities with respect to

both inner and outer bypass duct annulus regions due to the local drop in P_0. This is a favourable flow feature as it leads to reduced skin-friction on the bypass duct walls. However, a mid-loaded distribution with high magnitude of non-uniformity (Fig. 2(a)) may result in excessive P_0 drop near the annulus walls. This may eventually cause flow-separation with a penalising influence on exhaust performance. Furthermore, Fig. 3(c) shows that the deployment of a mid-loaded profile has significantly altered the transonic shock-field downstream of the bypass nozzle exit relative to the case of uniform inflow shown in Fig. 3(a). The bypass flow over the core cowl appears to form a shock cell that consists of a supersonic core that is enveloped by high-Mach number subsonic boundaries. The shock cell over the core after-body appears to comprise weak oblique shock waves and expansion fans, as well as a stronger normal shock downstream of the core cowl trailing edge. The observed normal shock produces entropy and leads to a further decrease in performance. However, the enveloping shock cell subsonic boundaries result in reduced shear-stress between the outer jet boundary and free-stream flow, as well as between the bypass and core cowl vent jet boundaries.

Fig. 3(d) presents the influence of the hub-loaded profile on the aerodynamic behaviour of the VHBR exhaust system. Similar to the case of the tip-loaded radial profile illustrated in Fig. 3(b), the deficit of P_0 at the fan OGV exit outer region has resulted in reduced flow momentum near the bypass duct outer annulus wall. This flow feature combined with the adverse pressure gradient generated due to the employment of a diffusive duct can lead to boundary layer separation at the duct outer annulus wall resulting in a performance penalty. More importantly, the formation of a double shock pattern can be observed on the core after-body almost immediately aft of the bypass nozzle exit. This is due to the increased P_0 near the inner bypass duct and nozzle annulus, combined with the high local curvature at the bypass nozzle inner wall downstream of the CP. The combined impact of these characteristics results in a flow over-acceleration near the inner annulus wall downstream of the nozzle exit. This causes the manifestation of a stronger shock-field leading to more intense shock-wave/boundary layer interaction phenomena. Moreover, the formation of a normal shock wave can be observed near the vicinity of the core after-body trailing edge.

Fig. 4 presents the effect of fan OGV exit profile on the aerodynamic performance of the exhaust system. Results are presented for $C_V^{Overall}$ and C_D^{Bypass} in Figs. 4(a) and (b), respectively. The obtained results are presented as percentage differences relative to the case of uniform inflow using the following expression:

$$\Delta C_V^{Overall}(\%) = 100 \times \frac{(C_V^{Overall})^{Non-uniform} - (C_V^{Overall})^{Uniform}}{(C_V^{Overall})^{Uniform}} \tag{6}$$

with a similar expression used for $\Delta C_D^{Bypass}(\%)$ in Fig. 4(b).

Fig. 4(a) shows that all investigated profiles result in a performance penalty in $C_V^{Overall}$ relative to the case of uniform inflow. The hub-loaded fan OGV exit profile resulted in the largest performance deficit with $\Delta C_V^{Overall}(\%) \approx -0.125\%$, whilst the mid-loaded radial profile appears be accompanied by a small penalty with $\Delta C_V^{Overall}(\%) \approx -0.006\%$. A significant negative impact in $C_V^{Overall}$ can also be observed for the tip-loaded profile with $\Delta C_V^{Overall}(\%) \approx -0.078\%$. The excessive performance penalty identified for the hub-loaded profile is attributed to the impact of two adverse flow features observed in Fig. 3(d): (a) the adverse shock topology on the core after-body, and (b) the separated flow region at the bypass duct outer annulus wall. With respect to the tip-loaded profile case, the predicted reduction in $C_V^{Overall}$ is attributed to the extended boundary layer separation region at the bypass duct inner annulus wall, as shown in Fig. 3(b). As regards the mid-loaded fan OGV exit profile, Fig. 3(c) shows that the negligible change in $C_V^{overall}$ can be attributed to two previously identified and conflicting flow characteristics: (a) the adverse effect of the normal shock downstream of the core after-body trailing edge, and (b) the favourable reduction in skin-friction at the bypass duct and nozzle walls, as well as the reduced shear-stress at the jet boundaries. It appears that the impact of these conflicting flow features on $C_V^{Overall}$ is of the same order of magnitude resulting in negligible performance change.

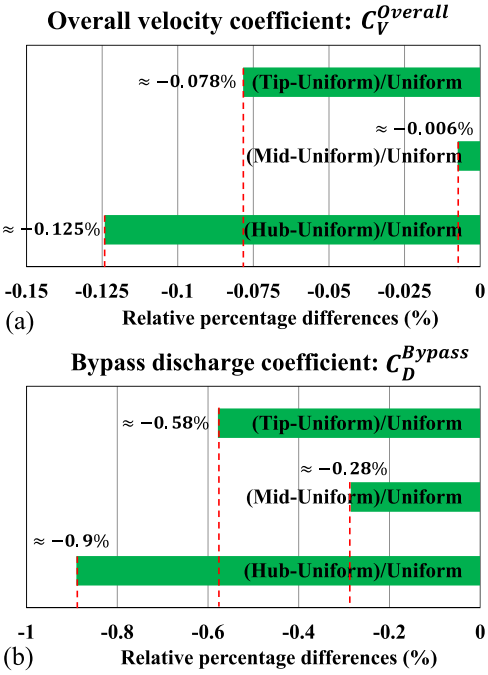

Fig. 4. Impact of fan exit profile on exhaust aerodynamic performance - comparison with uniform inflow scenario - Eq. (6): (a) $\Delta C_V^{Overall}(\%)$ and (b) $\Delta C_D^{Bypass}(\%)$.

Further to the above, Fig. 3(c) shows that the near-wall velocity in the vicinity of the bypass inner and outer annulus walls has been reduced substantially for the mid-loaded fan profile case. Further reduction in near-wall velocity, for example due to FNPR decrease or due to external flow suppression, can lead to flow-reversal near the vicinity of the inner and outer bypass duct annulus walls. This can result in an increase of total pressure loss within the bypass duct, as well as in $C_V^{Overall}$ deficit.

Fig. 4(b) shows that the predicted changes in C_D^{Bypass} are almost an order of magnitude larger compared to those identified for $C_V^{Overall}$. This is attributed to the local momentum deficit near the bypass duct and nozzle annulus walls which renders the boundary layer growth more sensitive to adverse pressure gradients. This affects the boundary layer thickness at the nozzle exit and consequently on C_D^{Bypass}. Furthermore, changes to the near-wall static pressure and temperature due to the imposed $P_0(r)$ and $T_0(r)$ variations affect the boundary layer Reynolds number which influences its thickness at the nozzle exit.

The hub-loaded profile has the largest impact on C_D^{Bypass} with $\Delta C_D^{Bypass}(\%) \approx -0.9\%$. This is followed by the tip-loaded profile with $\Delta C_D^{Bypass}(\%) \approx -0.58\%$, whilst the mid-loaded profile appears to be the most benign with $\Delta C_D^{Bypass}(\%) \approx -0.28\%$. The hub-loaded distribution results in the largest C_D^{Bypass} deficit due to the unchoked flow region at the bypass nozzle exit outer annulus wall which is dominant due to the axi-symmetric topology of the domain. The impact noted for the tip-loaded profile is attributed to the low Mach number at the bypass nozzle exit inner annulus line

Table 2
Design space bounds for fan exit profile parameters.

Design variable	Lower bound	Upper bound	Unit
$\frac{P_0^{max}}{P_0^{avg}}$	1.0	1.08	–
$r_{P_0}^{max}$	0.25	0.75	–
$\frac{T_0^{max}}{T_0^{avg}}$	1.0	1.08	–
$r_{T_0}^{max}$	0.25	0.75	–
θ_{sw}^{avg}	0.0	5.0	deg

which results in significant boundary layer thickness. Finally, the mid-loaded profile case has the smallest impact on C_D^{Bypass} due to the relatively high-subsonic Mach number at the inner and outer bypass annulus walls at the nozzle exit.

At this point it is re-iterated that the values of $\Delta C_D^{Bypass}(\%)$ are significant and can reach up to -0.9% for the hub-loaded profile, relative to the case of uniform inflow. Although the changes noted in C_D^{Bypass} do not directly affect exhaust performance, they influence the required bypass nozzle geometric throat area for a given mass-flow rate demand [3,9,41]. Therefore, for a given $\Delta C_D^{Bypass}(\%)$, the bypass nozzle throat area would have to be re-scaled relative to the case of uniform inflow in order to satisfy the engine mass-flow requirement for the designated operating condition. These changes in C_D^{Bypass} could be of interest from the point of view of exhaust system size, structure, and weight, but they should also be considered relative to the associated manufacturing tolerances. To conclude, changes in C_D^{Bypass} should also be accounted for alongside changes in $C_V^{Overall}$ during the design and analysis of the exhaust system.

3.2. Fan exit profile effect: DSE and analysis

Following the identification of the governing flow mechanisms, a DSE was carried out to understand the response of the inflow design space. Numerical analyses were performed for the baseline exhaust geometry (Fig. 3) where the design space consisted of the spatial variation of $P_0(r)$ and $T_0(r)$ at the bypass entry. A non-parametric fan exit profile was used in the DSE [14]. The impact of area-averaged swirl angle θ_{sw}^{avg} was also included in the design space through scaling the bespoke swirl profile accordingly. This resulted in an inflow representation comprising a total of five (5) variables as noted in Table 2.

The LHD method [31] was initially deployed to discretise the fan exit profile design space described in Table 2. A global database was compiled consisting of 250 inflow combinations in terms of $P_0(r)$, $T_0(r)$, and θ_{sw}^{avg}, using the parametric profile definition described in section 2.3 of this article. The performance of the baseline exhaust system (Fig. 3) was evaluated for each of the derived $P_0(r)$, $T_0(r)$, and θ_{sw}^{avg} combinations using the CFD approach described and validated by the authors [41].

It is noted that a consistent fan OGV exit profile representation requires that the radial variations of $P_0(r)$ and $T_0(r)$ are interrelated through the span-wise distribution of isentropic efficiency of the fan blade and OGV. However, during the preliminary design of the exhaust system, sufficiently accurate fan efficiency data may not available to establish a proper correlation between the radial variations of $P_0(r)$ and $T_0(r)$. Thus, a generic approach is required that can be applied independently of fan-efficiency related attributes. Therefore, for the compilation of the inflow database, the radial profiles of $P_0(r)$ and $T_0(r)$ were treated as independent flow parameters. This was done to extract orthogonal information from the aerodynamic design space in order to separate, identify,

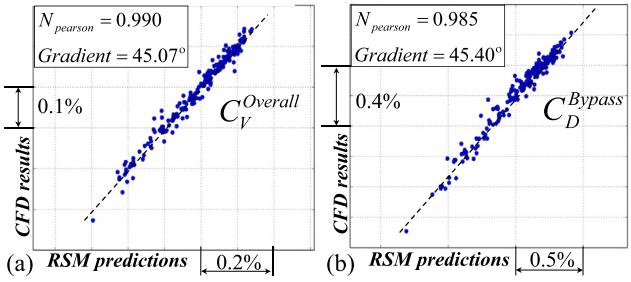

Fig. 5. LOO cross-validation applied to the fan exit profile RSMs structured for: (a) $C_V^{Overall}$ and (b) C_D^{Bypass}.

and model the fundamental flow mechanisms associated with the impact of $P_0(r)$ and $T_0(r)$, independently. Hence, the employed approach ensures that the derived surrogate-models will be able to describe the impact of the associated flow-mechanisms in a separate manner. Moreover, it allows a bounded RSM interrogation of the form of $P_0(r) = f\left(T_0(r), \theta_{sw}^{avg}\right)$ which ensures compatibility between the employed inflow definition and realistic flow conditions.

The obtained results were subsequently utilised to structure RSMs that can approximate the response of the design space. The approach employed in this paper was based on interpolation using Gaussian Processes Regression [32]. The classical LOO cross-validation method [9,10] was utilised to assess the quality of the RSMs. The process is illustrated in Figs. 5(a) and (b) for $C_V^{Overall}$ and C_D^{Bypass}, respectively. It can be observed that the computed values of $N_{Pearson}$ when correlating RSM predictions with CFD results are of the order of 0.990 and 0.985 for $C_V^{Overall}$ and C_D^{Bypass}, respectively. The computed quality metrics indicate the excellent predictive accuracy of the structured RSMs.

A systematic RSM interrogation was carried out to understand the aerodynamic response of the inflow design space. The RSM interrogations were carried out in terms of $P_0(r)$ radial profiles through direct control of $\left(\frac{P_0^{max}}{P_0^{avg}}\right)$ and $r_{P_0}^{max}$. A fixed ratio of $\frac{P_0^{max}/P_0^{avg}}{T_0^{max}/T_0^{avg}} = 0.995$ was assumed along with coincident radial positions of peak flow quantities $r_{P_0}^{max}$=$r_{T_0}^{max}$ to ensure compatibility between the radial distributions of T_0 and P_0 during the analyses carried out. The assumption behind this approach was that the impact of fan blade span wise loading variation on its radial distribution of isentropic efficiency was not significant enough to de-couple the radial profiles of P_0 and T_0 at the fan exit. Furthermore, a constant area-averaged swirl angle was assumed of $\theta_{sw}^{avg} \approx 2^{\circ}$.

Fig. 6 illustrates the impact of fan exit flow profile in terms of $\frac{P_0^{max}}{P_0^{avg}}$ and $r_{P_0}^{max}$ on the aerodynamic performance of the baseline exhaust system. Results are presented for $C_V^{Overall}$, C_D^{Bypass}, and C_D^{Core} in Figs. 6(a), (b), and (c), respectively. It can be observed that all metrics have clearly defined optimum inflow regions. As mentioned in section 3.1, the baseline exhaust geometry was pre-optimised for $C_V^{Overall}$ using a nearly mid-loaded fan OGV exit flow profile with $\left(\frac{P_0^{max}}{P_0^{avg}}\right) \approx 1.02$ and $r_{P_0}^{max} \approx 0.52$ [11]. However, Fig. 6(a) suggests that the optimum inflow region for $C_V^{Overall}$ is obtained for $\left(\frac{P_0^{max}}{P_0^{avg}}\right) \approx 1.04$ and $r_{P_0}^{max} \approx 0.52$, which is 2% more intense compared to the profile for which the exhaust geometry was optimised. This alludes to the potential to obtain further exhaust

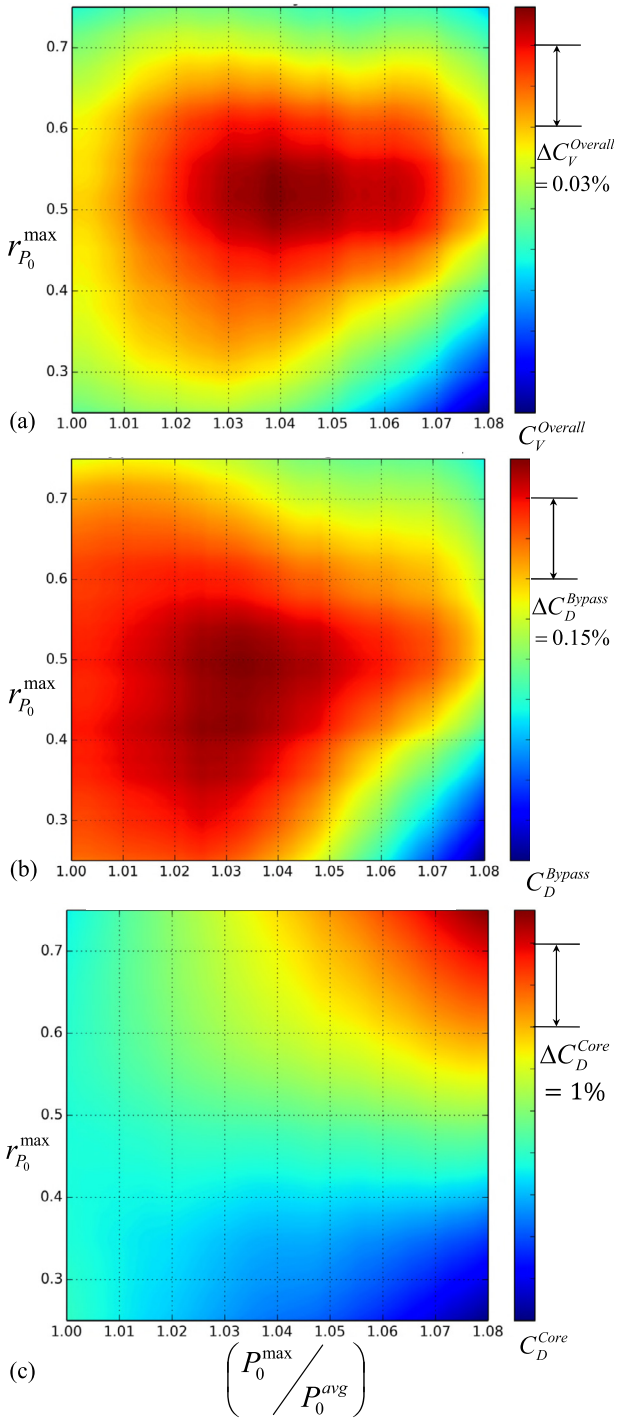

Fig. 6. RSM interrogation results – impact of fan exit flow profile on exhaust aerodynamic performance for the baseline exhaust geometry (Fig. 3): (a) $C_V^{Overall}$, (b) C_D^{Bypass}, and (c) C_D^{Core}.

performance improvements if the exhaust geometry is optimised in tandem with the employed fan exit profile, instead of using a fixed inflow definition. Furthermore, it can be noted that the inflow region with the largest performance deficit is associated with intense hub-loaded profiles with $\left(\frac{P_0^{max}}{P_0^{avg}}\right) \geq 1.06$ and $r_{P_0}^{max} \leq 0.35$. This is due to the associated adverse flow features described in section 3.1.

Fig. 6(b) presents a similar behaviour with respect to the impact of fan OGV exit flow profile on C_D^{Bypass} with clearly defined

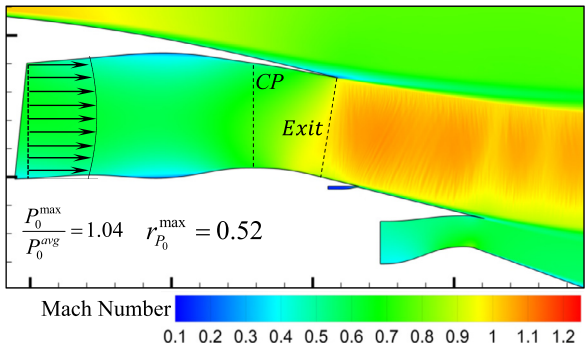

Fig. 7. Impact of optimum fan exit profile on the baseline exhaust aerodynamic behaviour.

favourable and adverse inflow domains. The optimum inflow region for C_D^{Bypass} is obtained for $\frac{P_0^{max}}{P_0^{avg}} \approx 1.035$ and $r_{P_0}^{max} \approx 0.5$ which is close to that identified for $C_V^{Overall}$. A 0.75% penalty in C_D^{Bypass} relative to the case of optimum inflow is observed near the vicinity of the hub-loaded inflow due to the unfavourable flow phenomena within the bypass duct and nozzle shown in Fig. 3(d).

The impact of fan OGV exit flow profile on C_D^{Core} is presented in Fig. 6(c). It can be observed that C_D^{Core} exhibits a substantially different behaviour compared to that noted for $C_V^{Overall}$ and C_D^{Bypass}. Due to the low value of CNPR ($CNPR \approx 1.5$) the core nozzle is unchoked. As a result, the core nozzle mass flow and C_D^{Core} are sensitive to the static pressure field in the vicinity of the core nozzle exit. For a tip-loaded profile ($r_{P_0}^{max} > 0.5$), Fig. 3(b) shows that the static pressure at the core nozzle exit is reduced due to the low $P_0(r)$ content near the inner bypass annulus wall and downstream core after-body causing near-wall subsonic flow conditions. Consequently this leads to an increase in core nozzle mass flow and C_D^{Core}. However, considering a hub-loaded $P_0(r)$ distribution ($r_{P_0}^{max} < 0.5$), Fig. 3(d) reveals the formation of a strong normal shock at the core after-body trailing edge. The observed normal shock causes a static pressure rise at the core nozzle exit with a concurrent reduction in C_D^{Core}. The observed behaviour appears to be amplified with increasing profile non-uniformity magnitude in terms of $\left(\frac{P_0^{max}}{P_0^{avg}}\right)$.

Fig. 7 presents the effect of optimum fan exit profile on the aerodynamic behaviour of the baseline exhaust. Analysis was carried out using the optimum inflow parameters for $C_V^{Overall}$ extracted from the RSM-based map shown in Fig. 6(a). It can be observed that the magnitude of the unfavourable flow features previously observed in Fig. 3(a) for the case of uniform inflow has been reduced. Specifically, the presence of locally supersonic flow domains noted in Fig. 3(a) downstream of the CP near the inner annulus nozzle wall has been alleviated. Furthermore, a shock-free flow-field is observed within almost the entire vicinity of the core after-body. The near-wall velocities within the bypass duct and nozzle have been reduced resulting in lower skin-friction, whilst the strength of the oblique shocks and expansion fans downstream of the core after-body trailing edge has been ameliorated. The improvements in the exhaust flow-field depicted in Fig. 7 yield a performance benefit of approximately 0.06% in terms of $C_V^{Overall}$, relative to the case of uniform inflow.

3.3. Combined inflow and geometry optimisation

The results presented in section 3.2 suggested the potential to obtain further performance improvements if the exhaust geometry is optimised in tandem with the fan OGV exit profile. Within

this section, a novel approach is developed that enables the identification of optimum exhaust designs for designated fan loading types, as well as the simultaneous optimisation of the exhaust geometry in combination with the fan OGV exit flow characteristics. This was achieved by extending the DSE approach of GEMINI to include the bypass inflow control variables for $P_0(r)$ and $T_0(r)$ (Fig. 2) in conjunction with the exhaust geometry control variables [11].

The geometric exhaust design space comprised twelve (12) design variables used to establish an analytical representation of the LP exhaust and core after-body annulus. These included parameters that controlled the bypass duct and nozzle, the core after-body, and the core cowl vent. The employed parametric geometry definition and the associated design space bounds were described by Goulos et al. [11]. The fan OGV exit annulus areas and angles were held fixed to ensure geometric compatibility of the exhaust system with the engine fan case. The parametric definition of the inflow design space was identical to that used in section 3.2. This included a total of five (5) control variables for $P_0(r)$, $T_0(r)$, and θ_{sw}. Thus, the merging of the geometric and inflow parts of the design space lead to a global LP exhaust flow-path representation comprising seventeen (17) design variables.

The combined LP exhaust design space was subsequently discretised with the deployment of the LHD DOE approach [31]. A global data-base containing 935 combinations of bypass inflow and exhaust geometries was compiled. This established a densely populated design space with a sample size to variable number ratio equal to 55. The DOE results were utilised to formulate surrogate models using the Kriging method [32]. The LOO cross-validation [46] method was applied to evaluate the predictive quality of the RSMs. The values of $N_{Pearson}$ and linear regression line gradient when cross-correlating RSM predictions with CFD results for $C_V^{Overall}$, were 0.95 and 42.4°, respectively. The Root Mean Squate (RMS) model error for $C_V^{Overall}$ was estimated to be 0.03%, which is close to the numerical accuracy of the employed CFD approach [41].

After establishing confidence in the predictive capability of the RSMs, they were employed to guide the optimisation process. Four (4) types of optimisation were performed: (i) a single (1) combined optimisation where both the inlet profile and the exhaust geometry were varied simultaneously to obtain the globally optimum LP system, and (ii) three (3) fixed inlet-profile geometric optimisations where for each case the bypass inflow distribution was held constant and the exhaust geometry was optimised. With respect to case (ii), optimisations were carried out for the tip, mid, and hub-loaded profiles outlined in Table 1.

The NSGA-II algorithm [33] was employed for all optimisations carried out. $C_V^{Overall}$ was set as the objective function to be maximised. The population size was set to be 20 times the number of variables. This resulted in a population size of 340 designs per generation. A convergence criterion of 10^{-20} was imposed on the average consecutive mutations per generation. A fixed value of $\theta_{sw} \approx 2^{\circ}$ was used during all optimisations carried out.

Fig. 8 presents the aerodynamic behaviour of the optimum exhaust geometries. Fig. 8(a) depicts the exhaust flow-field for the combined inflow and geometry optimisation scenario, whilst Figs. 8(b), (c), and (d) present numerical predictions for the tip, mid, and hub-loaded variants, respectively. The associated impact on $C_V^{Overall}$ and C_D^{Bypass} is presented in Figs. 9(a) and (b), respectively. Results are presented as percentage differences relative to the combined profile and geometry optimisation case, which was treated as a "best case scenario", as follows:

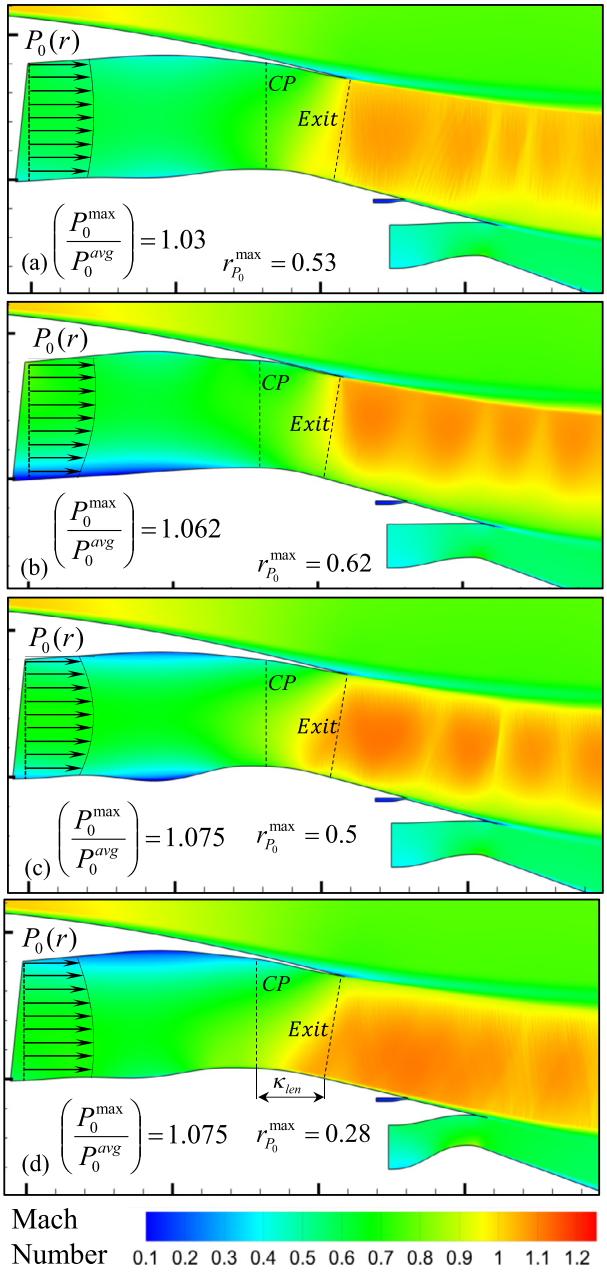

Fig. 8. Impact of fan exit profile on exhaust aerodynamics – optimised exhaust geometries: (a) combined inflow and geometry optimisation, (b) tip-loaded, (c) mid-loaded, and (d) hub-loaded.

$$\Delta C_V^{Overall}(\%) = 100 \times \frac{(C_V^{Overall})^{Hub/mid/tip} - (C_V^{Overall})^{Combined}}{(C_V^{Overall})^{Combined}} \tag{7}$$

with a similar expression used for the definition of $\Delta C_D^{Bypass}(\%)$.

Fig. 8(a) shows that with respect to the combined inflow and geometry optimisation case, the optimum exhaust shape is similar to the baseline geometry of Fig. 3. Furthermore, it can be observed that the globally optimum inflow characteristics are obtained for $\left(\frac{P_0^{max}}{P_0^{avg}}\right) \approx 1.03$ and $r_{P_0}^{max} \approx 0.53$. These are comparable to the values associated with the non-parametric inflow definition, $\left(\frac{P_0^{max}}{P_0^{avg}}\right) \approx 1.02$ and $r_{P_0}^{max} \approx 0.52$, employed by Goulos et al. for the optimisation of the baseline exhaust shape [11]. Thus, the

similarity between the fan exit profile used in the previous optimisation of the baseline exhaust [11] and the obtained optimum $P_0(r)$ distribution, resulted in comparable exhaust geometries for the baseline (Fig. 3) and optimised cases (Fig. 8(a)).

A notable geometric alteration shown in Fig. 8(a) relative to the baseline exhaust, is associated with the axial position of the core cowl vent on the core after-body. Specifically, the optimisation resulted in a core cowl vent exit location of nearly 40% of core cowl length downstream relative to where it was positioned on the baseline geometry (Fig. 3). This is attributed to the relative insensitivity of the post-bypass-nozzle exit transonic flow-field to the core cowl vent placement for the combined case due to the local $P_0(r)$ deficit. The combined optimisation yielded a $C_V^{Overall}$ improvement of 0.07% relative to the case of uniform inflow. In terms of C_D^{Bypass}, the combined optimisation case (Fig. 8(a)) exhibits an improvement of approximately 0.17% relative to the case of uniform inflow (Fig. 3(a)). This is attributed to the reduced skin-frictions losses within the bypass duct for the combined optimisation case. This is due to the optimisation of the fan exit profile which resulted in non-uniform distributions of $P_0(r)$ at the bypass inlet leading to reduced near-wall velocities.

Fig. 8(b) shows that with respect to the tip-loaded fan OGV exit profile, substantial modifications were applied to the exhaust geometry to better align the aerodynamic behaviour of the exhaust with the prescribed inflow distribution. Specifically, the employment of higher core after-body angle can be observed in combination with nearly-zero gradient at the nozzle CP within the outer bypass annulus wall. However, some of the adverse flow features previously observed in Fig. 3(b) have not been mitigated. These include the low momentum region near the inner annulus wall of the bypass duct and the downstream subsonic flow region at the nozzle throat. However, these flow mechanisms are linked to the imposed distribution of $P_0(r)$. As such, it is unlikely that a geometric optimisation would be able to alleviate these flow phenomena unless the fan OGV exit area constraint was relaxed. Fig. 9(a) shows that the tip-loaded optimised exhaust exhibits a $C_V^{Overall}$ deficit of the order of -0.13% relative to the combined optimisation result. The change in $C_V^{Overall}$ obtained relative to the baseline exhaust is 0.013% which is small. This is attributed to the previously noted adverse flow phenomena associated with the imposed $P_0(r)$ distribution.

With regards to the mid-loaded profile optimum geometry, Fig, 8(c) shows that small geometric modifications have been applied relative to the baseline exhaust geometry (Fig. 3(c)). As a result, the flow phenomena are nearly identical between the two cases. Fig. 9(a) shows that the combined optimisation result outperforms the mid-loaded optimised exhaust in terms of $C_V^{Overall}$ by 0.075%. This is due to the geometric similarity between the two exhaust geometries.

Fig. 8(d) shows that the aerodynamic behaviour of the exhaust geometry optimised for the hub-loaded inflow distribution has been substantially improved. Specifically, the adverse shock-field on the core after-body previously observed in Fig. 3(d) has been alleviated. This has been achieved by increasing the nozzle length ratio κ_{len}^{in} and by relaxing the curvature distribution at the inner annulus wall downstream of the bypass nozzle CP. This modification allows the under-expanded bypass nozzle jet to align more gradually with the core after-body angle before expanding to supersonic conditions. This lowers the magnitude of flow over-acceleration due to the locally excess values of $P_0(r)$ near the inner annulus. Concurrently, the local maximum Mach number downstream of the bypass nozzle exit is reduced which mitigates the adverse shock topology noted previously on the core after-body of the baseline exhaust (Fig. 3(d)).

However, despite the beneficial impact of the optimisation on the exhaust flow-field, Fig. 9(a) shows that a performance penalty

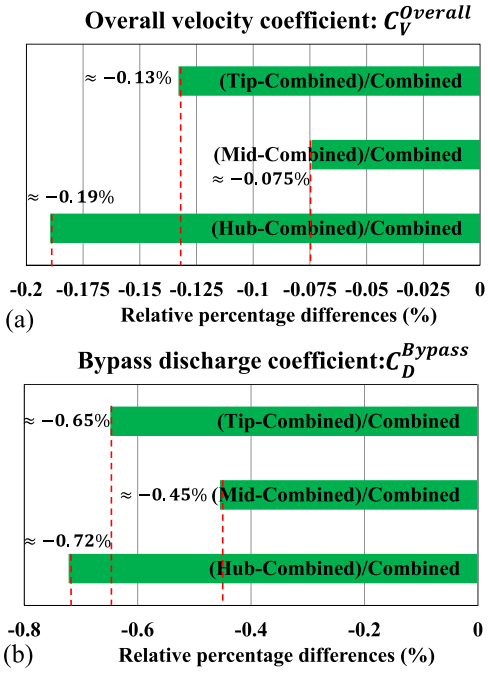

Fig. 9. Impact of fan exit profile on exhaust performance for optimised geometries - comparison with combined geometry and inflow optimisation scenario - Eq. (7): (a) $\Delta C_V^{Overall}$(%) and (b) ΔC_D^{Bypass}(%).

remains in terms of $C_V^{Overall}$ for the hub-loaded optimum exhaust which reaches -0.19% relative to the combined optimisation scenario. The baseline and hub-loaded optimum designs exhibit similar performance when coupled to the prescribed hub-loaded inflow distribution. However, the variable bounds imposed on the parametric definitions of $P_0(r)$ and $T_0(r)$ during the optimisation process have skewed the design towards the most aerodynamically favourable part of the design space.

Fig. 9(b) presents the associated percentage differences in exhaust performance in terms of C_D^{Bypass}. The results demonstrate that the fixed-inflow optimum exhausts exhibit substantial penalties in terms of C_D^{Bypass} relative to the combined optimisation scenario shown in Fig. 8(a). These are of the order of -0.65%, -0.45%, and -0.72% for the tip, mid, and hub-loaded profile optimised geometries, respectively. However, although not shown in Fig. 9(b), the tip and hub-loaded profile optimised geometries (Figs. 8(b) and (d)) exhibit substantial C_D^{Bypass} improvement when compared to the baseline exhaust for the associated inflow distributions (Fig. 3(b) and (d)). These reach approximately 0.1% and 0.33% for the tip and hub-loaded variants, respectively, and are due to the flow mechanisms described in section 3.1. These predicted increases in C_D^{Bypass} indicate that the combined optimisation has resulted in an exhaust system that can satisfy the engine mass-flow rate demand with a decreased geometric throat area, as demonstrated by the values of ΔC_D^{Bypass} shown in Fig. 9(b), relative to the fixed-inflow optimisation cases. Thus, the combined optimisation process could also lead to the design of an exhaust system with reduced size and weight, which could result to further performance gains at engine level

At this point, it is emphasised that the developed approach aims to yield propulsive efficiency improvements through optimisation of the LP exhaust flow-path. However, changes applied to fan blade loading inevitably have an impact on fan isentropic efficiency, which has a consequent effect on thermal efficiency. Hence, a holistic engine optimisation method should account for the impact of fan blade loading on both thermal as well as on propulsive efficiency, and as such, it should target the optimisation of engine

Specific Fuel Consumption (SFC) instead of only $C_V^{Overall}$. However, such an approach would require accurate estimates of fan isentropic efficiency for each assessed variation of fan blade span-wise loading (Fig. 2). Furthermore, this analysis would require knowledge on exchange rates between fan isentropic efficiency and SFC, as well as between $C_V^{Overall}$ and SFC [48]. However, this topic falls outside the scope of the present work which is on the LP exhaust flow-path design only. Hence, further elaboration on this analysis aspect shall be omitted.

4. Conclusions

This paper described the development and application of a novel methodology for the LP exhaust flow-path optimisation of civil aero-engines during the stages of preliminary design. A parabolic mathematical definition was formulated to parameterise and control the circumferentially-averaged radial distributions of P_0 and T_0 at the fan OGV exit. The devised formulation was implemented into a validated tool for the aerodynamic analysis and optimisation of separate-jet exhaust systems.

It was shown that the combined geometry and inflow LP exhaust flow-path optimisation can offer substantial performance benefits compared to a strictly geometric fixed-inflow design approach. The improvement in $C_V^{Overall}$ for the combined inflow and geometry optimisation was found to be of the order of 0.13%, 0.075%, and 0.19%, relative to the fixed-inflow optimised exhausts for the tip, mid, and hub-loaded fan OGV exit profiles, respectively. The hub-loaded inflow distribution was found to incur the largest performance penalty when compared to the mid and tip-loaded variants. The fixed-inflow geometric optimisations carried out were able to ameliorate adverse flow-phenomena related to the influence of the bypass inlet conditions. Furthermore, the associated gains in C_D^{Bypass} were found to be approximately 0.65%, 0.45%, and 0.72%, relative to the tip, mid, and hub-loaded fixed-inflow optimum exhausts, respectively. The predicted increases in C_D^{Bypass} could potentially have an impact on the exhaust system size, structure, and weight, when exceeding manufacturing tolerances, as they could reduce the geometric throat area required to satisfy the engine mass-flow rate demand. The developed method can derive exhaust design definitions based on the optimum aerodynamic coupling between the exhaust and fan loading characteristics.

Data statement

Due to commercial confidentiality agreements the supporting data is not available.

Declaration of Competing Interest

There is no conflict of interest.

Acknowledgements

This project was funded by Innovate UK (grant number TSB 113075).

References

[1] A.H. Epstein, Aeropropulsion for commercial aviation in the twenty-first century and research directions needed, AIAA J. 52 (5) (May 2014) 901–911.
[2] A. Guha, Optimum fan pressure ratio for bypass engines with separate or mixed exhaust streams, AIAA J. Propuls. Power 17 (5) (September-October 2001) 1117–1122.
[3] I. Goulos, T. Stankowski, J. Otter, D. MacManus, N. Grech, C. Sheaf, Aerodynamic design of separate-jet exhausts for future civil aero-engine, part 1: parametric geometry definition and CFD approach, ASME J. Eng. Gas Turbines and Power 138 (8) (August 2016) 081201.
[4] AGARD, Aerodynamics of Power Plant Installation, Advisory Group for Aerospace Research and Development, AGARD-CP-301, 7 Rue Ancelle 92200 Newilly, Sur Seine, France, May 1981.
[5] M.H. Robinson, D.G. MacManus, K. Richards, C. Sheaf, Short and slim nacelle design for ultra-high BPR aero-engines, in: 55th AIAA Aerospace Sciences Meeting, Grapevine, Texas, USA, 2017, p. 1.
[6] T. Stankowski, D.G. MacManus, M. Robinson, C.T. Sheaf, The aerodynamic effects of a VHBR engine installation to the common research model, J. Aircr. 54 (6) (June 2017).
[7] B. Malouin, J.-Y. Trepanier, E. Laurendeau, Installation and interference drag decomposition via RANS far-field methods, Aerosp. Sci. Technol. 54 (7) (2016) 132–142.
[8] C.E. Hughes, G.G. Podboy, R.P. Woodward, R.J. Jeracki, The effect of bypass nozzle exit area on fan aerodynamic performance and noise in a model turbofan simulator, in: National Aeronautics and Space Administration, TM-2013-214029, Reno, Nevada, June 6-9, 2005, December 2013.
[9] I. Goulos, J. Otter, T. Stankowski, D. MacManus, N. Grech, C. Sheaf, Aerodynamic design of separate-jet exhausts for future civil aero-engines, part 2: surrogate modeling and optimisation, ASME J. Eng. Gas Turbines and Power 138 (8) (August 2016) 081202.
[10] I. Goulos, T. Stankowski, D. MacManus, P. Woodrow, C. Sheaf, Civil turbofan engine exhaust aerodynamics: impact of bypass nozzle after-body design, Aerosp. Sci. Technol. 73 (2) (2018) 85–95.
[11] I. Goulos, J. Otter, T. Stankowski, D. MacManus, N. Grech, C. Sheaf, Design optimisation of separate-jet exhausts for the next generation of civil aero-engines, in: Proceedings of the 23rd International Symposium of Air-Breathing Engines ISABE 2017, No. ISABE-2017-21407, Manchester, UK, 03-08, September 2017.
[12] B.D. Keith, K. Uenishi, D.A. Dietrich, CFD-based three-dimensional turbofan exhaust nozzle analysis system, AIAA J. Propuls. Power 9 (6) (November-December 1993) 840–846.
[13] A.J. Peace, A method for calculating afterbody flows, J. Propuls. Power 13 (4) (July-August 1987) 357–364.
[14] F. Bucci, Effect of Non-Uniform Inflow on the Aerodynamic Behavior of Separate-Jet Exhausts for Civil Aero-Engines, Master's thesis, Cranfield University, Bedford, UK, 2016.
[15] D. Dusa, D. Lahti, D. Berry, Investigation of subsonic nacelle performance improvement concept, in: 18th Joint Propulsion Conference, Cleveland, OH, U.S.A, June 21-23, 1982, pp. 21–23.
[16] S.G. Mida, Guide to In-Flight Thrust Measurement of Turbojets and Fan Engines, Advisory Group for Aerospace Research and Development, 7 Rue Ancelle 92200 Newilly, Sur Seine, France, January 1979.
[17] E.E. Covert, C.R. James, W.M. Kimsey, G.K. Rickey, E. Rooney, Thrust and Drag: Its Prediction and Verification, Progress in Astronautics and Aeronautics Series, American Institute of Aeronautics & Astronautics, Reston, VA, 1985.
[18] J. Zhang, Z. Zhou, W. Wei, Y. Deng, Aerodynamic design of an ultra-low rotating speed geared fan, Aerosp. Sci. Technol. 63 (4) (2017) 73–81.
[19] X. Tang, J. Luo, F. Liu, Adjoint aerodynamic optimisation of a transonic fan rotor blade with localized two-level mesh deformation method, Aerosp. Sci. Technol. 72 (1) (2018) 262–277.
[20] X. Tang, J. Luo, F. Liu, Aerodynamic shape optimisation of a transonic fan by an adjoint-response surface method, Aerosp. Sci. Technol. 68 (9) (2017) 26–36.
[21] C. Clemen, P. Albrecht, S. Herzog, Systematic optimisation of a turbofan bypass duct system, in: ASME Turbo Expo 2012: Turbine Technical Conference and Exposition, No. GT2012-68276, Copenhagen, Denmark, June 11-15, 2012.
[22] B.L. Lapworth, HYDRA-CFD: a framework for collaborative CFD development, in: International Conference on Scientific and Engineering Computation (ICSEC), Singapore, June 30-July 02, 2004.
[23] I.M. Sobol, On the systematic search in a hypercube, SIAM J. Numer. Anal. 16 (5) (October 1979).
[24] G.B. Wright, Radial Basis Function Interpolation: Numerical and Analytical Development, Ph.D. thesis, Department of Applied Mathematics, University of Colorado, USA, 2003.
[25] D. Sasaki, S. Obayashi, K. Nakahashi, Navier-Stokes optimisation of supersonic wings with four objectives using evolutionary algorithm, J. Aircr. 39 (4) (July-August 2002) 621–629.
[26] T. Tschirner, M. Pfitzner, R. Merz, Aerodynamic optimisation of an aeroengine bypass duct OGV-pylon configuration, in: Proceedings of ASME Turbo Expo 2002: Power for Land, Sea, and Air, Amsterdam, the Netherlands, June 3-6, 2002, pp. 3–6.
[27] P.R. Spalart, S.R. Allmaras, A one-equation turbulence model for aerodynamic flows, Rech. Aérosp. 1 (1994) 5–21.
[28] W.K. Anderson, J.L. Thomas, D.L. Whitfield, Multigrid acceleration of the flux-split Euler equations, AIAA J. 26 (6) (June 1988) 649–654.
[29] Ansys Inc, 275 Technology drive, Canonsburg, PA 15317, ANSYS ICEM CFD Tutorial Manual.
[30] Ansys Inc, 275 Technology drive, Canonsburg, PA 15317, ANSYS FLUENT User's Guide.
[31] A. Olsson, G. Sandberg, O. Dahlblom, On latin hypercube sampling for structural reliability analysis, Struct. Saf. 25 (1) (2003) 47–68.

[32] H. Bayraktar, F. Turalioglu, A kriging-based approach for locating a sampling site in the assessment of air quality, Stoch. Environ. Res. Risk Assess. 19 (2005) 301–305.
[33] K. Deb, A. Pratap, S. Agarwal, T. Meyarivan, A fast and elitist multiobjective genetic algorithm: NSGA-II, IEEE Trans. Evol. Comput. 6 (2) (April 2002) 182–197.
[34] W.L. Macmillan, Development of a Module Type Computer Program for the Calculation of Gas Turbine Off Design Performance, Ph.D. thesis, Department of Power and Propulsion, Cranfield University, 1974.
[35] B.M. Kulfan, Recent extensions and applications of the 'CST' universal parametric geometry representation method, Aeronaut. J. 114 (1153) (March 2010) 157–176.
[36] F. Zhu, N. Qin, Intuitive class/shape function parameterization for airfoils, AIAA J. 52 (1) (January 2014) 17–25.
[37] V. Pachidis, P. Pilidis, L. Marinai, I. Templalexis, Towards a full two dimensional gas turbine performance simulator, Aeronaut. J. 111 (1121) (2007) 433–442.
[38] D.C. Wilcox, Comparison of two-equation turbulence models for boundary layers with pressure gradient, AIAA J. 31 (8) (August 1993) 1414–1421.
[39] I. Ansys, ANSYS FLUENT theory guide: Release 16.2, ANSYS, Canonsburg, PA, 2013.
[40] W. Sutherland, The viscosity of gases and molecular forces, Philos. Mag. 36 (1893) 507–531.
[41] J. Otter, I. Goulos, D. MacManus, M. Slaby, Aerodynamic analysis of civil aero-engine exhaust systems using computational fluid dynamics, AIAA J. Propuls. Power 34 (5) (2018) 1152–1165.
[42] J. Bird, Higher Engineering Mathematics, 6th ed., Taylor & Francis Group Ltd, 2010, 11 New Fetter Ln, London EC4A 1AG.
[43] E.J. Gunn, C.A. Hall, Loss and deviation in windmilling fans, J. Turbomach. 138 (10) (2016).
[44] N.A. Cumpsty, J.H. Horlock, Averaging nonuniform flow for a purpose, J. Turbomach. 128 (1) (2006) 120–129.
[45] Jeracki, R. J., Comprehensive report of fan performance from duct rake instrumentation on 1.294 pressure ratio, 806 ft/sec tip speed turbofan simulator models, NASA Glenn Research Center, TM-2006-213863, February 2016.
[46] R. Kohavi, A study of cross-validation and bootstrap for accuracy estimation and model selection, in: Proceedings of the Fourteenth International Joint Conference on Artificial Intelligence, Vol. 2, 1995, pp. 1137–1143.
[47] Haselback, F., Newby, A., and Parker, R., Next Generation of Large Civil Aircraft Engines - Concepts & Technologies, European Turbomachinery Conference, Madrid, Spain, 23-27 March 2015..
[48] P. Walsh, P. Fletcher, Gas Turbine Performance, Blackwell Publishing, 2004.

2019-05-17

Civil turbofan engine exhaust aerodynamics: impact of fan exit flow characteristic

Goulos, Ioannis

Elsevier

Goulos I, MacManus D, Sheaf C. Civil turbofan engine exhaust aerodynamics: impact of fan exit flow characteristics. Aerospace Science and Technology, Volume 93, October 2019, Article number 105181

https://doi.org/10.1016/j.ast.2019.05.033